Supersonic Testing of 0.8 m Disk Gap Band Parachutes in the Wake of a 70 deg Sphere Cone Entry Vehicle

Anita Sengupta*
Jet Propulsion Laboratory, California Institute of Technology, Pasadena, CA

Mark Wernet†, James Roeder‡, Richard Kelsch§
NASA Glenn Research Center, Cleveland, OH

Al Witkowski**
Pioneer Aerospace, South Windsor, CT

and

Thomas Jones††
NASA Langley Research Center, Hampton, VA

Supersonic wind tunnel testing of Viking-type 0.8 m Disk-Gap-Band (*DGB*) parachutes was conducted in the *NASA* Glenn Research Center 10'x10' wind-tunnel. The tests were conducted in support of the Mars Science Laboratory Parachute Decelerator System development and qualification program. The aerodynamic coupling of the entry-vehicle wake to parachute flow-field is under investigation to determine the cause and functional dependence of a supersonic canopy breathing phenomenon referred to as area oscillations, characteristic of *DGB*'s above Mach 1.5 operation. Four percent of full-scale parachutes (0.8 m) were constructed similar to the flight-article in material and construction techniques. The parachutes were attached to a 70-deg sphere-cone entry-vehicle to simulate the Mars flight configuration. The parachutes were tested in the wind-tunnel from Mach 2 to 2.5 in a Reynolds number range of $2x10^5$ to $1x10^6$, representative of a Mars deployment. Three different test configurations were investigated. In the first two configurations, the parachutes were constrained horizontally through the vent region to measure canopy breathing and wake interaction for fixed trim angles of 0 and 10 degrees from the free-stream. In the third configuration the parachute was unconstrained, permitted to trim and cone, similar to free-flight (but capsule motion is constrained), varying its alignment relative to the entry-vehicle wake. Non-intrusive test diagnostics were chosen to quantify parachute performance and provide insight into the flow field structure. An in-line load-cell provided measurement of unsteady and mean drag. Shadowgraph of the upstream parachute flow field was used to capture bow-shock motion and wake coupling. Particle image velocimetry provided first and second order flow field statistics over a planar region of the flow field, just upstream of the parachute. A photogrammetric technique was used to quantify fabric motion using multiple high speed video cameras to record the location in time and space of reflective targets placed on the canopy interior. The experimental findings including an updated drag model and the physical basis of the area oscillation phenomenon will be discussed.

Nomenclature

d	=	Capsule diameter
D_o	=	Parachute nominal diameter
x/d	=	Non-dimensional trailing distance measured from capsule to parachute band leading edge
d/D_o	=	Capsule to parachute nominal diameter ratio
Re	=	Reynolds number

* Senior Engineer, *EDL* and Advanced Technologies, 4800 Oak Grove Dr, MS 301-440C, Senior Member.
† Senior Research Engineer, Optical Instrumentation and NDE Branch, 21000 Brookpark Rd, Associate Fellow
‡ Mechanical Facility Engineer, FTD/Aeropower & Propulsion Test Engineering Branch, 21000 Brookpark Rd.
§ Aerospace Engineer, Applied Structural Mechanics Branch, 21000 Brookpark Rd.
** Director Engineering Operations, 45 S. Satellite Rd., Member AIAA.
†† Senior Engineer, Optical Diagnostics Branch, Member AIAA.

ω_{AO}	=	Frequency of area oscillations
A_p	=	Projected area variation
t_{FI}	=	Time to full inflation
t^*	=	Non-dimensional time
Q	=	Dynamic Pressure
DGB	=	Disk Gap band
FSI	=	Fluid Structure Interaction
CFD	=	Computational Fluid Dynamics
MSL	=	Mars Science Laboratory
PIV	=	Particle Image Velocimetry

I. Introduction

The Mars Science Laboratory (*MSL*) is *NASA*'s next landed mission to Mars. The mission will deliver to the surface a 900 kg rover equipped with instruments to analyze the atmosphere and soil. To improve science return a more ambitious entry-descent-and landing (*EDL*) subsystem has been developed, enabling access to higher altitude landing sites with challenging surface terrain and with greater precision than previously demonstrated[1]. The *MSL EDL* system leverages the technologies and architectures developed for Viking, MER and Phoenix missions and pushes the envelope of the existing heritage in terms of the induced aero-thermodynamic environment [2]. The *MSL EDL* system utilizes a lifting-body entry, active RCS control, 4.5-m entry-vehicle, 21.5-m meter supersonic parachute, and a retro-propulsive terminal descent system with a tethered touch-down[3] (Fig. 1). The resultant architecture yields an error ellipse of 10 km from the designated surface target, truly advancing the state-of-the-art [4,5.]

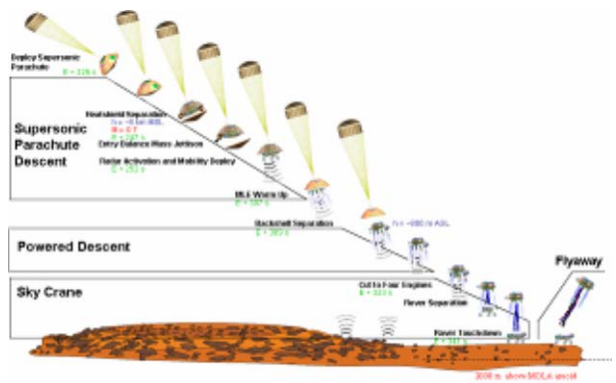

Fig 1. *MSL* descent and landing sequence indicating the parachute function in the heat shield separation even and power-descent initiation[10].

The parachute decelerator system is a major element of the *MSL EDL* system providing a highly scalable, volume, and mass efficient source of aerodynamic drag. The *MSL* parachute is a 21.5-m nominal diameter Viking heritage disk-gap-band design (*DGB*) [6]. The Viking program qualified a 16.1-m nominal diameter *DGB* parachute over a range of deployment conditions up to and including 750 Pa and Mach2.2[7,8,9]. All *NASA* Mars missions since the Viking Lander have flown *DGB*'s less than 16 m in diameter and deployed at less than Mach 2, to take advantage of the existing supersonic qualification[10]. *MSL*, however, will fly a 21.5-m parachute deployed up to Mach 2.3, a departure from the existing heritage qualification. Moreover, the *MSL* parachute will spend up to 10 seconds above Mach 1.5, an area of concern due to a known aerodynamic instability that has been observed on multiple flight and wind tunnel tests of *DGB*'s deployed above Mach 1.5 [11,12,13]. This instability, commonly referred to as "area oscillations" by the parachute community, is a supersonic canopy breathing mode characterized by periodic in-folds in the band, leading to localized canopy collapse and subsequent re-inflation. The area oscillation subjects the parachute to projected area variation, drag instability, and a re-inflation load on the order of the peak inflation load. The cause of the phenomenon has not been understood for the past several decades and therefore a better understanding was required for the *MSL* parachute qualification effort for parachute performance and health considerations. Recent work with a rigid *DGB* parachute supersonic test and corresponding *CFD* simulations has yielded a great deal of insight into this phenomenon, specifically its dependence on the aerodynamic coupling of the entry-vehicle wake to parachute bow-shock, laying the ground work for a flexible parachute test program[14,15].

Supersonic wind tunnel tests of 4% scale *MSL* parachutes were conducted in support of the *MSL* parachute supersonic qualification program[16]. These tests investigated the aerodynamic coupling of the entry-vehicle wake to parachute flow-field to determine the cause, functional dependence, and scaling of the supersonic area oscillation phenomenon. Results have been used to determine the frequency of the instability, dynamic drag variation, and provide an update to the Mach efficiency curve for Viking-type *DGB* parachutes from Mach 2.0 to 2.5. The test

program was also designed to generate a validation dataset for fluid-structure interaction computational tools under development for *MSL*[17]. It builds from a prior test program and Computational Fluid Dynamics (*CFD*) validation effort that utilized a 2.1% scale rigid *MSL* parachute with an entry-vehicle to explore the aerodynamic flow-field of Mars parachute deployments[14,17]. Results and findings from the test will be discussed herein.

Table 1. 4% scale *DGB* parachute-with-capsule test matrix[23].

		High *Q*		Low *Q*					
Configuration	**Mach**	***Re*** **(x10^6)**	***Q*** **(kPa)**	***Re*** **(x10^5)**	***Q*** **(kPa)**	**Trim (deg)**	***d/D$_o$***	***D$_o$ (m)***	***x/d***
Constrained	2	1.0	16.8	2.0	4.3				
	2.2	1.1	18.3	2.4	3.8	0	0.21	0.8	10.6
	2.5	1.2	19.8	2.5	3.1				
Constrained	2	1.0	16.8	2.0	4.3				
	2.2	1.1	18.3	2.4	3.8	10	0.21	0.8	10.6
	2.5	1.2	19.8	2.5	3.1				
Unconstrained	2	1.0	16.8	2.0	4.3				
	2.2	1.1	18.3	2.4	3.8	variable	0.21	0.8	10.6
	2.5	1.2	19.8	2.5	3.1				

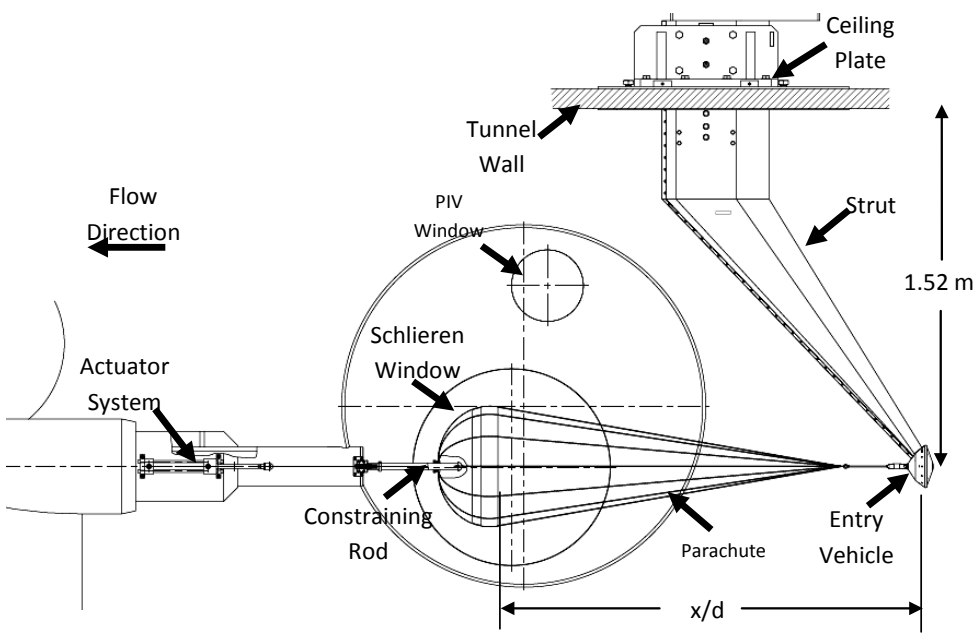

Fig 2. Schematic of flexible test configuration in the *GRC* 10x10 supersonic wind tunnel.

II. Test Description

A. Wind Tunnel Test Configuration

The parachute test was conducted in the *GRC* 10x10 closed-loop supersonic wind tunnel. The test section has a 10x10x40 ft (3x3x12 m) geometry with smooth walls and standard air as the operating fluid. Mach number in the tunnel is controlled with a flexible-wall nozzle geometry enabling Mach 2 to 3.5 operation. Variable pressure operation enabled matching the Mars deployment Reynolds number range of 1x10^5 to 3x10^6. More details on the facility can be found in ref.18.

The test matrix was selected to explore the Mach, Reynolds number, dynamic pressure, and trim angle of a Mars deployment (Table 1). Matching Reynolds number and Mach number were deemed to be the most representative of a Mars deployment as *CFD* simulations of the parachute and entry-vehicle flow-field indicate the area oscillation phenomenon is turbulence dependent[17,19,]. Because of the small test article size, matching a flight-like *Re* necessitates high dynamic pressure (20 kPa). As this was an order of magnitude greater than the flight dynamic pressure, low dynamic pressure (4 kPa) runs were also performed. These were delineated as high *Q* and low *Q* runs, respectively. It should be noted that the low *Q* runs were still a factor of 4 higher than a flight-like deployment, but lower tunnel pressures could not be achieved with the exhaust system that was used for the test. Low *Q* runs were also required to increase parachute lifetime for the *PIV* measurement, as will be discussed later.

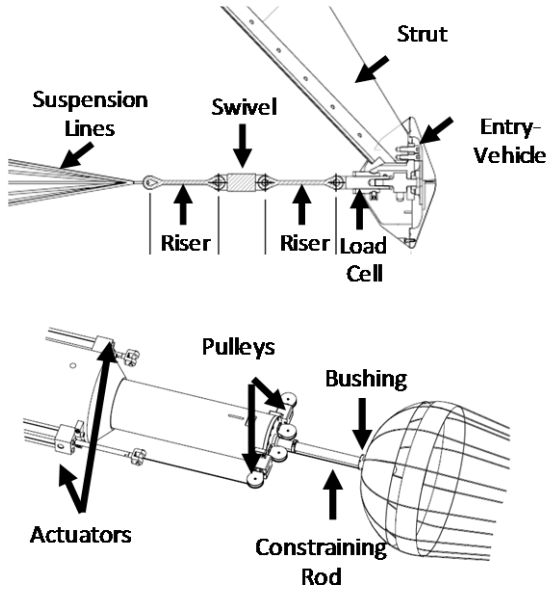

Fig 3. (Top) Parachute to capsule connection and (bottom) constrained parachute configuration[23].

A schematic of the test configuration is shown in Fig. 2. A 0.8 m nominal diameter *DGB* parachute with 0.17 m maximum diameter 70-deg sphere cone entry-vehicle at an *x/d*=10.6 was selected for the test program, providing a d/D_o of 0.21 [20]. This is equivalent to ~4% of flight-scale, and the maximum scale possible in the 10x10 to ensure reflected shocks intersected downstream of the parachute[23]. A swept-back diamond-wedge stainless steel strut was selected to mount the entry-vehicle to the tunnel ceiling. The strut was sized to prevent lateral vibrations at the same time minimizing aerodynamic interference or distortion of the entry vehicle's wake[17,14]. The entry-vehicle (capsule) was hard-mounted to the strut at a 0-deg angle of attack with respect to the free stream direction. The parachute was attached to the entry-vehicle via a swivel, two Kevlar risers, and a single-axis load-cell as shown in Fig. 3 (top). One riser was used to connect the load-cell to the swivel. The second riser was used to connect the swivel to the parachute triple bridle assembly. This combined metallic and textile joint provided three rotational and three translation degrees of freedom and a trailing distance of *x/d*=10.6 from the band leading edge to the capsule maximum diameter. The load-cell was hard-mounted inside of the entry-vehicle, preventing any applied moment to the internal strain gauges.

The test program explored three parachute configurations: a fixed 0-deg parachute trim angle, a 10-deg trim angle, and the parachute free to trim and cone unconstrained relative to the entry-vehicle. For the constrained test configuration the parachute was held to fixed trim angle via a constraining rod that passed through the canopy apex, as shown in Fig. 3 (bottom). The parachute was able to translate axially and rotate along the rod, but all lateral motions were prevented. The parachute interface was a metallic ring sewn to the vent and will be discussed in more detail later. The constraining rod was attached to the chamber balance mount. The balance mount can be configured to provide up to a 20-deg angle relative to the free-stream direction; providing the 0 and 10-deg trim configurations.

The test section has multiple optical access points as shown in Fig. 4 for the parachute test configuration. A pair of optical grade windows was used for Shadowgraph imaging of the parachute bow-shock. Two windows located just above the Schlieren windows provided access for the *PIV* cameras. The *PIV* laser sheet was fed through a window in the tunnel test section floor which provided a stream-wise plane upstream of the parachute from an *x/d* of 6 to 10. Two windows upstream of the entry-vehicle were used for high-speed video cameras and lighting. Two additional windows in the floor and ceiling upstream of the entry-vehicle provided vantage points for high-speed video footage of the parachute from the floor and ceiling. These diagnostics will be described in more detail later.

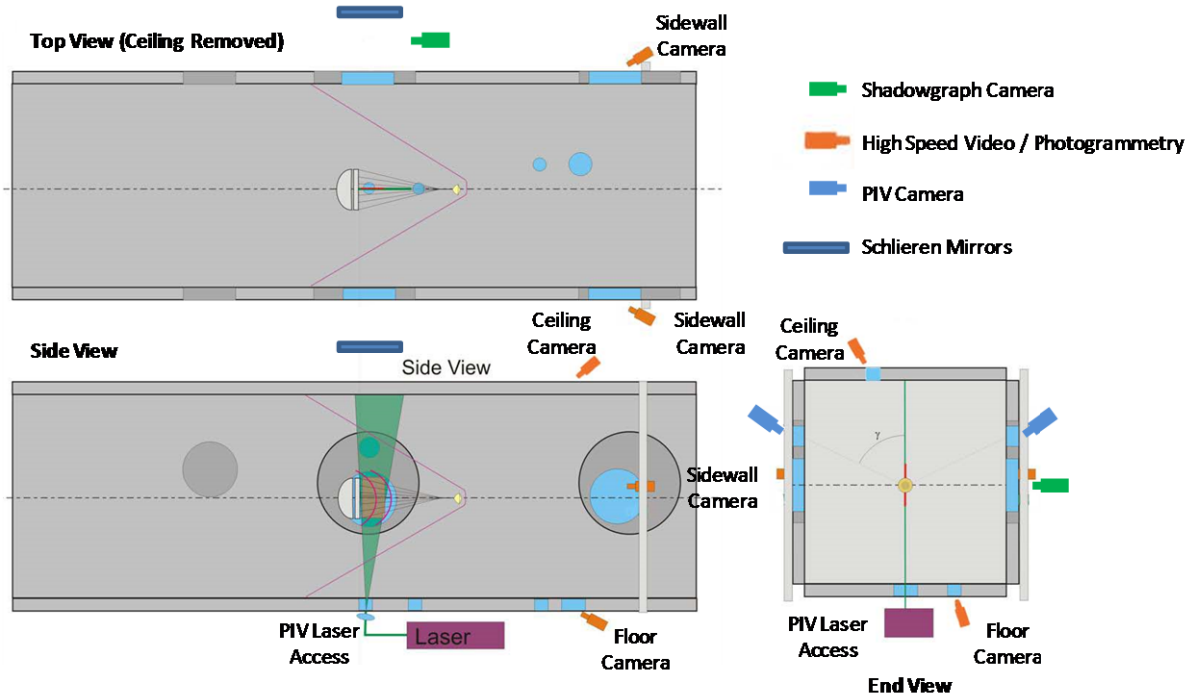

Fig. 4 Camera placement and optical diagnostics indicating high speed video, shadowgraph, and *PIV*.

Table 2. Subscale and full scale parachute parameters[23,10,6,21].

Parameter	**Subscale**	***MSL***
Nominal Diameter (D_o)	0.8 m	21.5 m
Projected Diameter (D_o)	0.67 D_o	0.67 D_o
Number of gores	24	80
Entry-vehicle / Nominal Diameter	0.21	0.21
Suspension Line Length	1.7D_o	1.7D_o
Suspension Line Thickness/D_o	0.0012	0.0002
Suspension Line Young's Modulus (GPa)	43.0	12.9
Canopy Fabric Young's Modulus (GPa)	0.88	0.69
Max Reynolds number (*Re*)	$1.2\text{x}10^6$	$1.0\text{x}10^6$
Mass Ratio ($m_p/\rho D_o^3$)	2	10
Max Dynamic Pressure (Pa)	$20\text{x}10^3$	750
Trailing Distance (x/d)	10.6	10.4

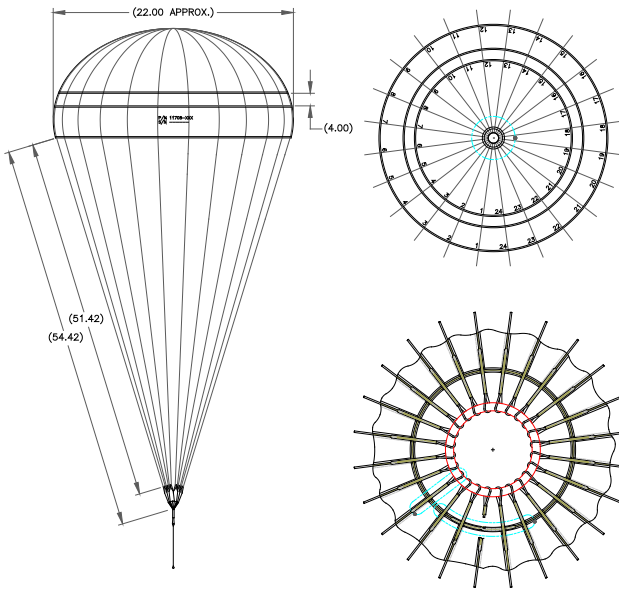

Fig. 5 Schematic showing (left) side view and (upper right) top down view and (lower right) detail of the vent region of the 0.8 m parachute[21].

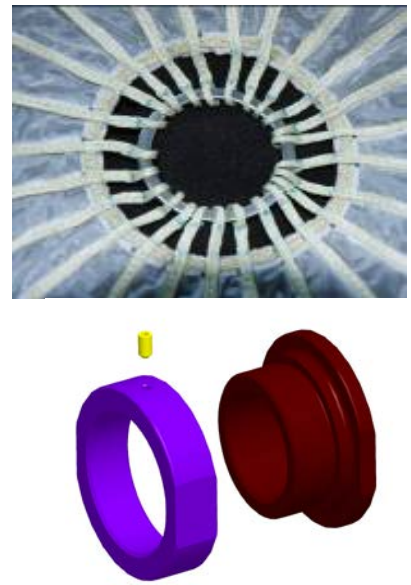

Fig. 6 (Top) Photograph of the apex region of the constrained parachute showing vent ring and vent line terminations. (Bottom) CAD drawing of vent bushing in the disassembled configuration[21].

B. Parachute Test Articles

The test articles were 0.8 m nominal (constructed) diameter *DGB* parachutes similar in construction to full-scale flight articles. Table 2 documents the relevant dimensions, material properties and non-dimensional scaling parameters of the test articles and compares them to the full-scale parachutes[21]. A schematic of the parachute is shown in Fig. 5. The test articles are geometrically scaled from the standard Viking-*DGB* configuration[6,8]. A 20 kPa dynamic pressure deployment necessitated the use of 1.15 oz/yd^2 Nylon and six times thicker than flight-scale Kevlar suspension lines[21]. The material scaling differences result in a factor of 3.3 and 1.3 times stiffer than the full-scale article for the canopy fabric and suspension lines respectively. The increased stiffness results in a more scalloped band leading-edge profile, as compared to the full-scale inflated shape. The effect on the parachute dynamic response is assumed to be second order for the mass ratios under examination[22]. Thicker suspension lines have the most significant effect on performance by increasing vent blockage and in the generation of shocks that can alter the subsonic wake's coupling to the parachute. These subjects are discussed in greater detail in section IV[23].

The constrained parachutes had a stainless steel vent-ring sewn into the apex of the canopy as shown in Fig. 6 (top). Each vent line terminates at the ring around which a smooth bore two-piece bushing was installed as shown in Fig. 6 (bottom). The constraining-rod allowed for free axial translation of the parachute. It was fitted with a hemispherical end-cap on the upstream-end to prevent the parachute from coming off. The vent area of the constrained parachutes was increased to account for geometric blockage due to the rod, and vent-ring, resulting in an effective open area equivalent to the standard Viking scale[21,23].

Deployment of the parachutes was challenging due to the separated flow startup environment of the 10x10 wind tunnel, prior to passage of the shock. Fabric test articles cannot survive this start-up flow environment, requiring a deployment mechanism to release the parachute after supersonic conditions were achieved [23]. A Spectra deployment sleeve was used to protect the parachute during startup (Fig. 7). The sleeve unlaced from the canopy apex to leading edge, to ensure removal of the sleeve prior to the onset of parachute inflation. The sleeve unlaced by means of a break-tied daisy chain rip-cord. The rip-cord was removed, on command, by a hydraulic actuator. A bungee loop, also tensioned by the same actuator, pulls the rip-cord away from the parachute after sleeve release (Fig. 8) [21].

C. Diagnostics

Non-intrusive diagnostics were selected to minimize interference with the wake structure and its interaction with the parachute. Shadowgraph of the parachute bow-shock region was obtained through optical windows on either side of the test article as shown in Fig. 2. Images were collected at 2000 fps to resolve the frequency of the parachute bow-shock oscillation. The camera had an *IRIG-B* time stamp to relate the image data collected to the rest of the data acquisition system output. The video data yield mean and *RMS* bow-shock shape and stand-off distance, as well as the frequency of oscillation. Shadowgraph images were also collected during inflation on some runs at a rate of 4000 fps. Prior testing with a rigid parachute indicated that Shadowgraph was the optimum interferometric technique to resolve the bow-shock[16].

Fig. 7 Photo of the parachute rigged in the deployment sleeve showing rip cord and lazy leg and mouth termination pin[23].

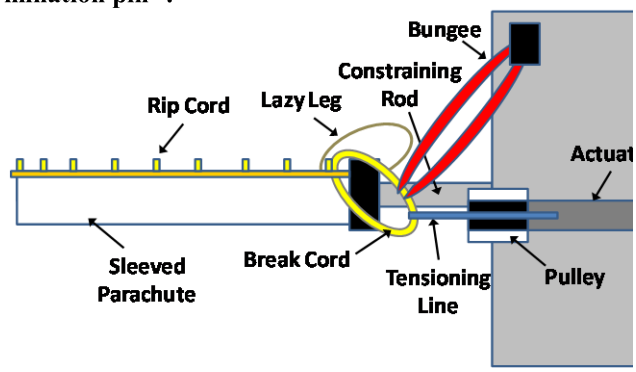

Fig. 8 Schematic of the parachute in the deployment sleeve showing textile connections. Following breakage of the break-cord the energy stored in the bungee pulls out the rip cord and deploys the parachute.

Drag was measured with a single-axis load-cell mounted within the entry-vehicle. Force was measured from the parachute single-riser through the swivel in the free-stream flow direction. Data were collected at 20 kHz by the tunnel data acquisition system. Drag is calculated in the same method as the Viking era wind tunnel programs for consistency [24].

$$C_D = \frac{F_D}{q\frac{1}{4}\pi D_o^2}$$

Dynamic pressure was not adjusted to account for tunnel blockage effects to be consistent with the method in ref.24. Tunnel blockage tends to drive up the "effective" dynamic pressure in the vicinity of the parachute and reduce the measured drag coefficient. For the 10 degree constrained case the cosine loss was factored into the measured value. It was also assumed there was zero frictional loss from the vent restraint bushing. For the unconstrained case, there was no correction for parachute trim and coning motion, as the angular motion was typically less than 10-deg and occurred at a relatively high frequency.

High-speed pressure transducers and static pressure ports were placed on the entry-vehicle back shell to provide mean and *RMS* pressures at known point locations. The transducers used the reference static-ports to define the absolute pressure.

Photogrammetric measurements of the canopy shape, utilizing high speed video, were made during the low *Q* and high *Q* runs with reflective targets placed on the canopy interior and band leading edge. Target's were applied with a thermally activated adhesive to the interior region and also tacked in place to the leading edge. Optimum canopy targeting pattern was determined during the course of the test. Some canopies were targeted only in the band and apex region. Other canopies were targeted throughout the disk region but those data have not yet been reduced due to their complexity. Targets were not placed on the canopy exterior as that would have made the shape reconstruction too difficult to compute due to overlap and lack of reference between interior and exterior targets. The canopies were illuminated by two 200 W Halogen lamps on either side of the chamber. The targets reflectivity and lighting were such that sufficient contrast could be provided to track the target locations from frame to frame of the high speed video. Four Photron SA1 high speed video cameras were used to collect images looking downstream, into the canopy. Two cameras were located on either sidewall of the test section looking through large optical grade windows. The remaining two camera views were through floor and ceiling windows. The camera layout is shown in

Fig. 4. A minimum of three camera views per instant in time were required to triangulate the parachute's position and then reconstruct its shape. Images were collected at 2000 fps and the cameras synchronized/triggered with respect to each other. Each camera had an *IRIG-B* time stamp to relate the image data collected to the rest of the data system output. The photogrammetric technique used three out of the four cameras. The fourth camera was used to capture the parachute inflation at 4000 fps or other features of interest and therefore was not synchronized with the other three cameras. This was determined on a test run basis.

Stereo particle image velocimetry (*PIV*)[25,26] was used to measure the three components of velocity in the parachute bow-shock region. The measurement was made over an axial plane centered in the tunnel, from the *x/d*=6 to *x/d*=10 position, intended to be aligned with the anticipated parachute bow-shock location. Figure 9 shows the *PIV* configuration including the location of the laser light sheet, cameras, and *PIV* data plane (relative to the parachute and entry-vehicle). Two high resolution cameras (4000x2672 pixels) were used to generate the cross correlation images from the illuminated region of the flow, providing a spatial resolution of 2.9 +/- 0.1 mm, over a 740x390 mm field of view [27]. *PIV* images were recorded at 2Hz for several minutes (test run specific), providing 600 to 1200 instantaneous measurements of the velocity field in this region. An *IRIG-B* time stamp was included with each instantaneous measurement, allowing reconstruction of the periodic / oscillatory motions in the flow by comparison to other data collected during the test (video, shadowgraph, drag).

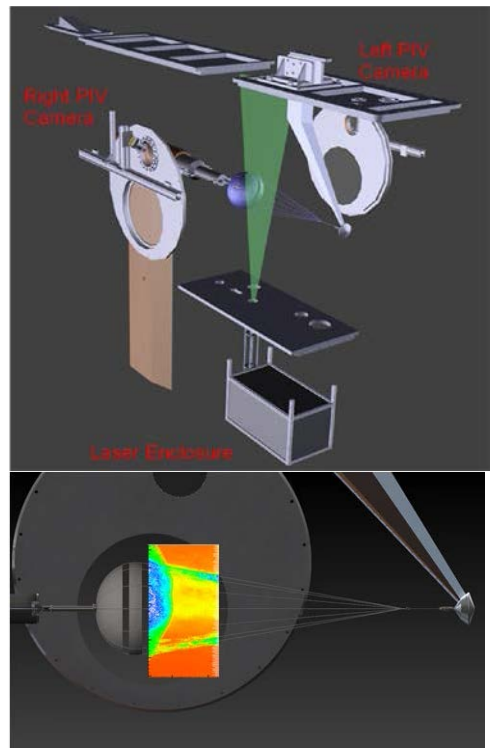

Fig. 9 (Top) *PIV* setup in the 10x10 facility. The laser sheet is shown in green. (Bottom) *PIV* velocity field measurement at Mach 2.2 for the 0 deg constrained configuration. The flow direction is from right to left in this image.

The processed *PIV* data included instantaneous and mean 3-component velocity, 3-component *RMS* velocity, and turbulence statistics [28]. For illustration, Fig. 9 (bottom) shows a mean axial velocity field *PIV* measurement overlaid in the physical space from where it was obtained for the 0-deg constrained parachute at Mach 2.2. This will be described in more detail in section III.

III. Experimental Results

A. Axial Force

The axial force measured by the single axis load-cell was used to compute the drag coefficient. Non-axial drag was not measured or included in the computation of drag. The drag coefficient versus Mach number is plotted in Fig. 10 for all three configurations investigated. The trend of decreasing C_D with Mach number is evident in the dataset. Also included on the figure are data obtained from the pre-Viking supersonic wind tunnel program of unconstrained subscale parachutes[24]. The measurements compare well with the Viking subscale dataset over the same Mach number range, utilizing the same data reduction technique. It is important to note that tunnel blockage and trailing distance effects were not included in the calculation of drag. This was done to provide consistency with measured drag from ref. 24. Qualitatively, tunnel blockage for the Viking dataset was higher than for *MSL*, which would tend to bring the two datasets closer together in terms of effective drag coefficient. However, the Viking data were from parachutes with an *x/d*=8.5 at a lower dynamic pressure, which could reduce the drag coefficient. As these parameters are not well understood in the supersonic environment, an adjustment for these factors has not been attempted.

The *RMS* drag is plotted against non-dimensional inflation time (t^*) in Fig. 11 for the 0-deg constrained case. Time is non-dimensionalized by the time from deployment to full inflation (t_{FI}) for each Mach number investigated (Table 3). *RMS* drag varied by as much as +/- 50% of the mean value. The *RMS* drag also indicates two dominant frequencies. It is likely the higher frequency component was driven by the bow-shock oscillation and the lower frequency component by the area oscillation instability. Another interesting finding from the *RMS* drag is that the peak drag load did not coincide solely with the initial inflation opening shock. Instead subsequent re-inflations during the area oscillation instability were characterized by peak loads within 2% of the initial inflation load. In a free flight application the parachute will decelerate the entry-vehicle and reduce the peak load from that of the initial inflation load. But from a structural loading perspective this does suggest the parachute will see a dynamic load factor similar to an opening shock augmentation. This may present additional difficulties with the traditional subsonic qualification of a supersonic parachute, as a single load application may not represent the full flight environment.

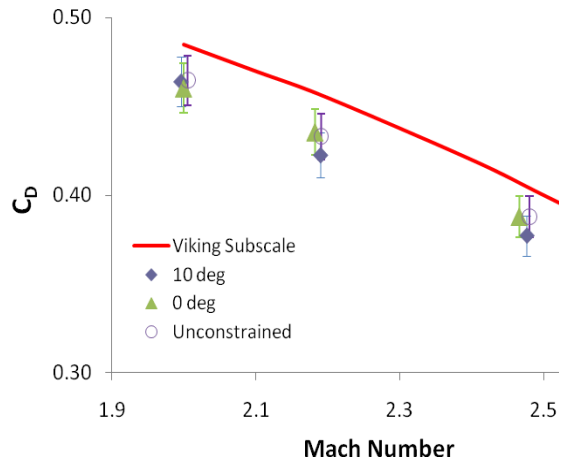

Fig. 10 Measured axial force for the three flexible parachute configurations tested. Error bars are only shown on the newly measured data. Subscale Viking-type *DGB* drag data from ref. 24 are shown for comparison.

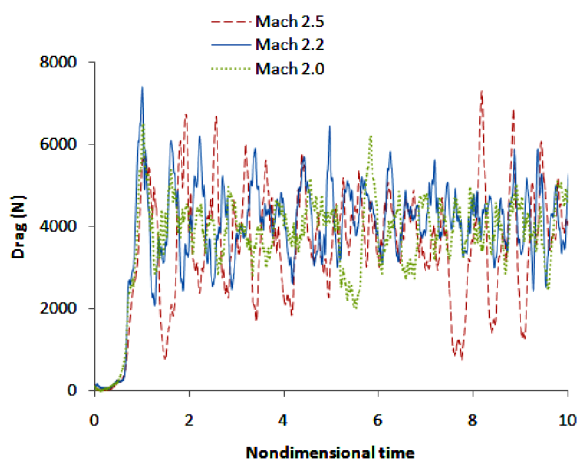

Fig. 11 *RMS* Drag Variation from Mach 2 to 2.5 for the 0-deg constrained parachute. Non-dimensional time is normalized by time to peak inflation for each dataset.

B. High Speed Video

The parachute fabric dynamics were directly reducible from the high speed video data. The fabric dynamics were characterized by periodic in-folds in the band region at times leading to canopy collapse and subsequent re-inflation events. The frequency associated with the in-folding was determined from high speed imaging. The frequency of the motion increased with Mach number from 2 to 2.5. The collapse and re-inflation events were characterized as area oscillations. The behavior is consistent with previous observations of the phenomena in the Viking and pre-Viking supersonic flight and wind tunnel programs. Area oscillations occurred at all three Mach numbers investigated. A representative oscillation at each Mach number tested is shown in Fig. 12 for the 0-deg constrained configuration. The collapse event was observed to propagate from the band leading edge inward towards the center of the canopy. The area oscillations were also characterized by the projected area variation and frequency associated with the collapse and subsequent re-inflation. These parameters were reduced from the digital images of each frame of the high-speed video during an oscillation event using a pixel count analysis and comparison between frames. The projected area variation (A_p) was observed to increase with Mach number and ranged from 46% to 68% (+/- 10%) of

Table 3. Parachute Video Data Analysis for the 0-deg constrained configuration

Test	Mach	ω_{AO} (Hz)	t_{fi} (ms)	$A_{p,min}$ (%)
0 deg	2	70	12.4	68
	2.2	81	11.5	52
	2.5	90	10.9	46

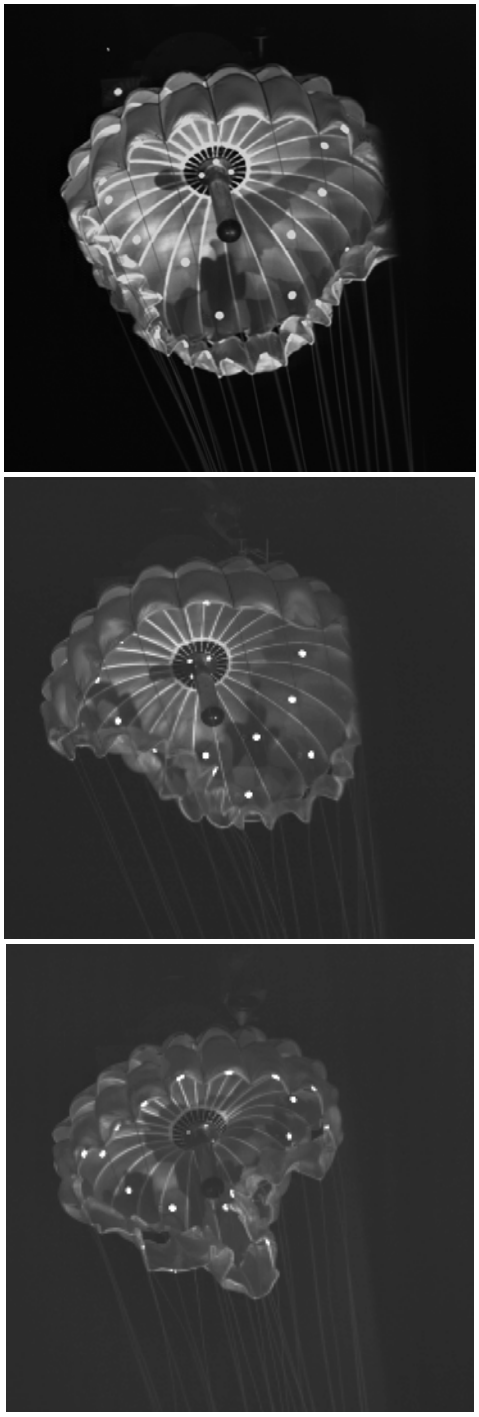

Fig. 12 Area oscillation at (top) Mach 2.0, (middle) Mach 2.2 and (bottom) Mach 2.5 for a 0-degree constrained 0.8 m *DGB* parachute.

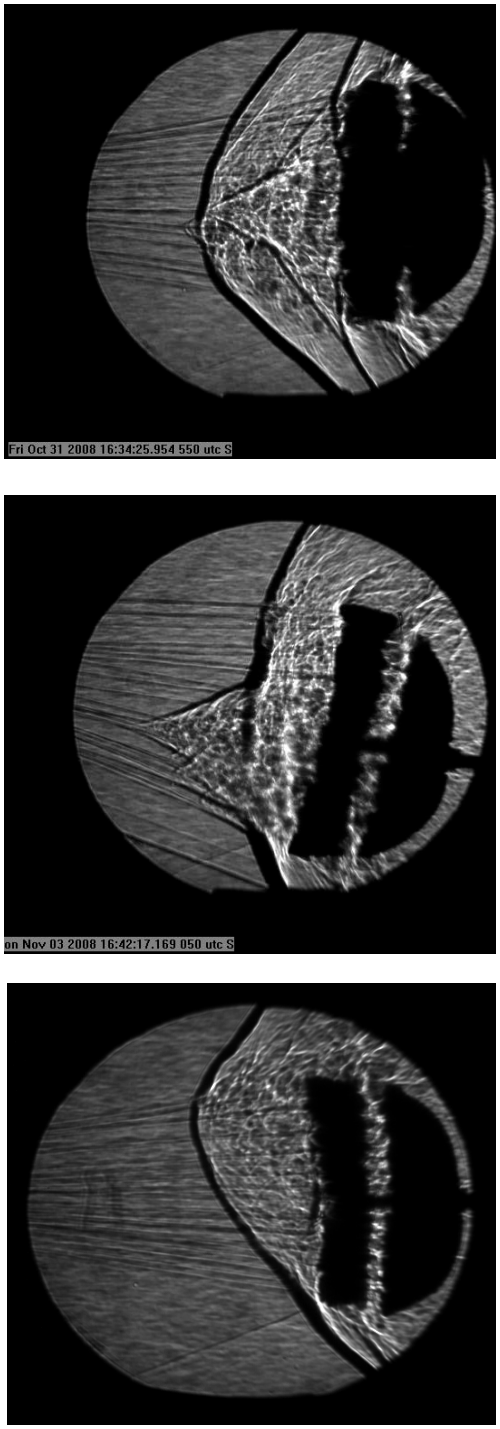

Fig. 13 Shadowgraph of an area oscillation at Mach 2.5 for (top) unconstrained and (middle) 10-deg constrained and (bottom) 0-deg constrained. These images correspond to an AO event. The flow direction is from left to right in the images.

full open during an oscillation event from Mach 2 to 2.5, respectively. It is important to note that the onset of an oscillation appeared to be random, however once an oscillation occurred, it was followed by 2 to 5 subsequent collapses and re-inflations with a prescribed period. The frequency associated with the subsequent oscillations was between 70 and 90 Hz (+/- 10 Hz) for Mach 2.0 to 2.5. Parameters reduced from the video data analysis are summarized in Table 3 for the 0-deg constrained configuration.

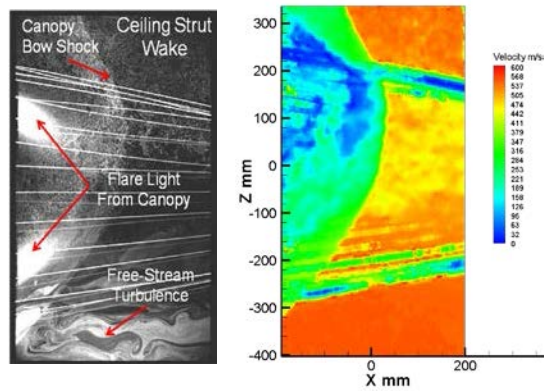

Fig. 14 *PIV* flow field measurement at Mach 2.2 for the 0-deg constrained configuration. (Left) Raw *PIV* image and (right) processed *PIV* velocity field magnitude which resolved the bow-shock, suspension line interaction, and capsule wake. The flow direction is from right to left in this image.

C. Shadowgraph

Shadowgraph imaging provided insight into the flow-field upstream of the parachute. The parachute bow-shock shape and stand-off distance varied in a cyclical fashion consistent with the unsteady parachute response and drag performance. The bow-shock varied from conical to detached and the parachute responded in kind for all Mach numbers investigated. The detached bow-shock state was related to nominal inflation. During this variation the pressure distribution in the canopy varied as evidenced by changes in the parachute's inflated shape (projected area). The extreme conical shock state was related to band in-folding. This suggests a pressurization and de-pressurization of the parachute interior determined by the bow-shock. Testing and computational fluid dynamics simulations of a rigid *DGB* parachute configuration exhibited a similar bow-shock temporal and spatial variation, suggesting the physical mechanism driving the instability is aerodynamic[14,17].

Shadowgraph images of the flow-field during an area oscillation are shown in Fig. 13 for Mach 2.5 operation of all three configurations (unconstrained, 10 deg, and 0-deg fixed trim). Compared to the fully inflated state, the shock is more conical, attached, and skewed by the collapsed state of the parachute mouth. The time resolved Shadowgraph imaging suggests a transition toward a shock ingestion, however this never occurred and instead the canopy re-inflates and pushes the shock back upstream.

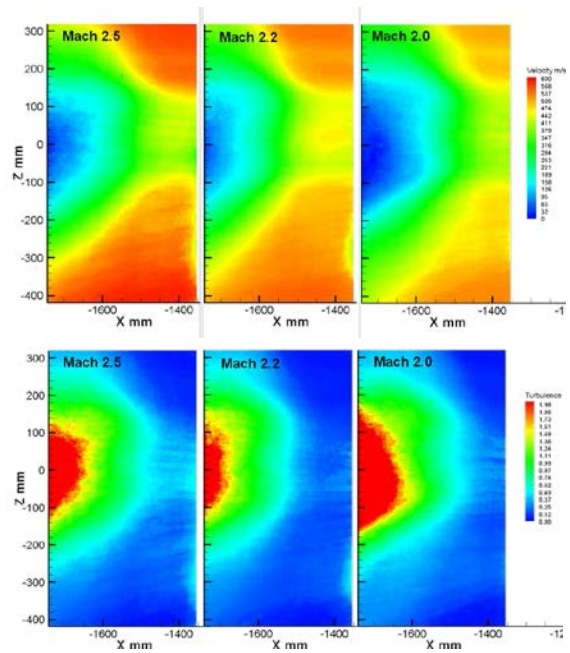

Fig. 15 *PIV* flow field measurements in the parachute bow-shock region for the unconstrained parachute configuration. The flow velocity is from right to left. (Left) ensemble averaged mean axial velocity in the bow-shock. (Bottom) Ensemble averaged turbulence measurement within the parachute bow-shock. The flow direction is from right to left in this image.

Several other features from the Shadowgraph imaging are worthy of discussion. In the fully inflated state, the bow-shock was asymmetric, which can be attributed to the ceiling strut contribution to the wake. At times, a pressure discontinuity or contact surface at the canopy mouth was observed, possibly established by mass flow into and out of the canopy. At other times, suspension line shocks were observed to disrupt the parachute bow-shock. This coincided with more violent fabric dynamics and will be discussed in the following section.

D. Particle Image Velocimetry

Instantaneous *PIV* measurements were collected and ensemble averaged for the low *Q* constrained and unconstrained runs. Figure 14 shows a raw *PIV* image and the reduced instantaneous velocity field map calculated

from it. The left hand image shows the seed material illustrating the bow-shock, capsule wake, and turbulence in the flow stream. The right hand image, a result of cross correlation of two instantaneous measurements, also indicates these features as well as the suspension line aerodynamic interference and quantitative measure of the velocity magnitude in the upstream of the canopy. The 2Hz instantaneous *PIV* flow field data were ensemble averaged to obtain mean and *RMS* three-component velocities and turbulence statistics. Figure 15 (top) is a comparison of the mean (ensemble averaged) axial velocity field in the parachute bow shock region at Mach 2.0, 2.2 and 2.5 for the unconstrained case. Figure 15 (bottom) is a comparison of the turbulence measured for the same conditions. The velocity varies from supersonic to subsonic in this region of the flow-field. The effect of the parachute's bow-shock coupling to the entry-vehicle is evident in the velocity field measurement with a column of low velocity flow connecting to the bow-shock. This is evident at all three Mach numbers. The bow-shock angle is also resolved by *PIV* with the most conical shock at Mach 2.5. Although not shown, the instantaneous *PIV* measurements captured the changing morphology of the bow-shock as it transits from conical to detached, similar to the shadowgraph. The fuzziness of the *PIV* images in Fig. 15 is due to the ensemble averaging of the canopy as it trims and cones about the *PIV* data plane. The constrained data have more refined bow-shock profiles for the mean case as their motion was restricted. Therefore, the instantaneous data are the most useful for comparing to the shadowgraph and high speed video for the unconstrained runs.

The *PIV* measurements also provide some insight into the aerodynamic interaction of the suspension lines with the parachute flow-field. *PIV* resolved what appeared to be an apparent creep of the bow-shock up the suspension lines. It should be noted, however, that the apparent decrease in flow velocity around the suspension lines is most probably caused by flare light from the suspension lines corrupting the cross correlations in these regions. The suspensions lines are typically not in the plane of the light sheet.

E. Photogrammetry

Post-test photogrammetric shape reconstruction from the high-speed video is underway with preliminary results presented below. Analysis to date suggests the highly dynamic motion of the canopy can result in overlap of individual reflective targets in the canopy interior. This leads to difficulty in automated reconstruction of the shape, and a hand-analysis of each frame must be performed. Post-test data reduction also revealed a frame rate of 2000 was sufficient to resolve the dynamic response of the parachute for the low *Q* runs but a higher frame rate for the high *Q* runs would have been preferred. Post-test findings also included target adhesion issues for the high *Q* runs, yielding only a few seconds of data before targets were lost.

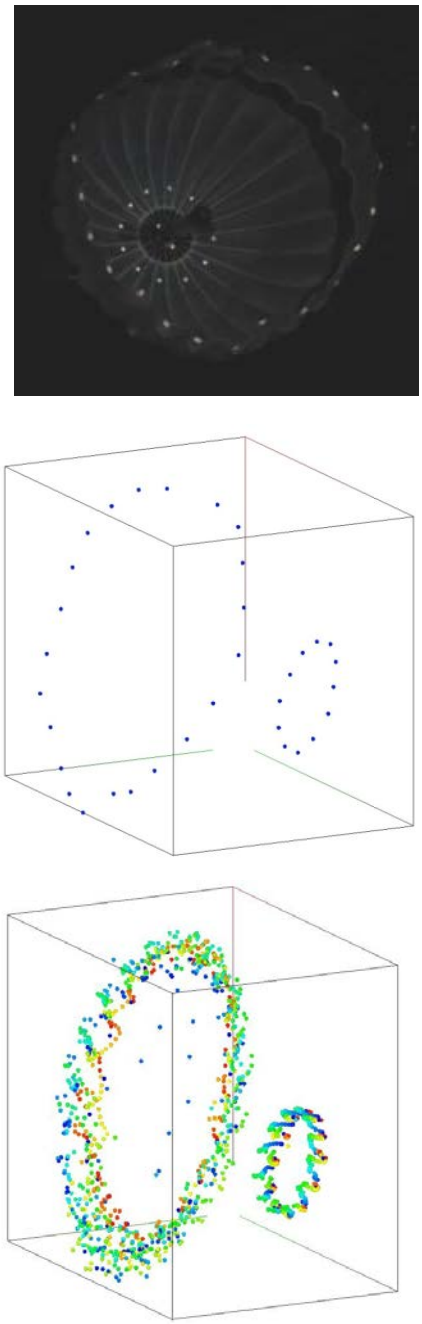

Fig. 16 Photogrammetric reconstruction of the band leading edge and canopy vent obtained from photo-reflective targets placed on the canopy interior and leading edge at Mach 2.5 for a 10-deg constrained run. (Top) Example of high-speed camera image of the inflated parachute. (Middle) Shape solution for a single frame reduced from three cameras. (Bottom) Multiple solutions of the parachute shape in time.

An example of the processed data is shown in Fig. 16 for a 10-deg constrained parachute at Mach 2.5 and low *Q*. The top image is a raw image from one of the three camera views. The middle image shows a single instance in time shape solution of the band leading edge and canopy apex at Mach 2.5. The bottom image shows multiple shape solution, each corresponding to a different instant in time. This dataset is an excellent quantitative measure of the projected area variation, canopy motion for computing angular rates, fabric dynamics for the purpose of code validation, and potentially canopy strain for the more heavily targeted canopies.

IV. Discussion

A. Mach Number

There was a clear Mach number dependence of all parameters measured in the test. Drag coefficient decreased with Mach number from 2 to 2.5. *RMS* drag increased with Mach number, which leads to structural implications for high Mach deployments. Qualitatively, the parachute lateral stability was affected by increasing Mach Shadowgraph data supports this trend as well. The parachute bow-shock morphology was more chaotic with increasing Mach, and the parachute canopy fabric responded in kind. These parachute responses to increasing Mach number affect the parachute performance and health, and should be factored into the overall *EDL* performance.

B. Dynamic Pressure versus Reynolds number

Dynamic pressure effects were coupled with a reduction in Reynolds number (turbulence) in the capsule wake, by definition. For the same Mach number, the lower dynamic pressure runs exhibited less severe area oscillations, smaller projected area fluctuation, and a fewer number of oscillation events. Similarly, the high *Re (Q)* runs had more dynamic lateral motion (trim). This confirms that the area oscillation phenomenon is turbulence driven. This was the case for both the thick and thin suspension lines. The high *Q* runs exhibited an increased *RMS* drag which has structural implications to the parachute.

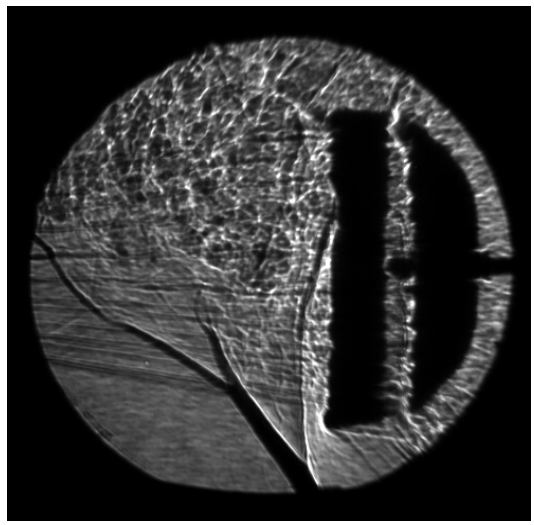

Fig. 17 Shadowgraph illustrating suspension line interaction and bow-shock disruption at Mach 2.0. The flow direction is from left to right.

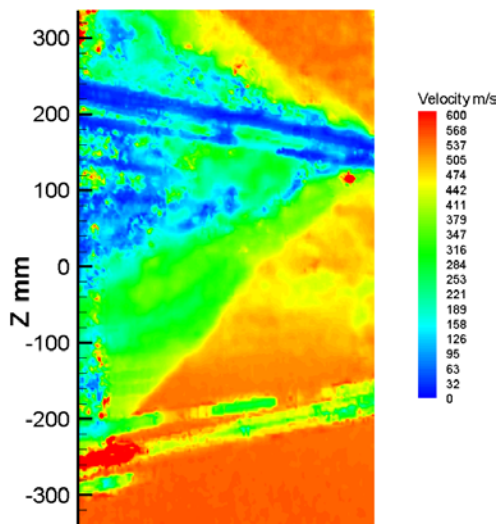

Fig. 18 *PIV* instantaneous velocity-field measurement indicating bow-shock crawling up the suspension lines. The flow direction is from right to left.

C. Suspension Line Interaction

As shown in Table 2, the subscale parachute lines are six times thicker, as compared to the full- scale parachute. Therefore, any suspension line effects will be more pronounced in the subscale configuration as compared to actual flight. Figure 17 is a shadowgraph image of the bow-shock region of the parachute during an unconstrained run to illustrate the suspension line interaction effect. Shocks from the suspension lines create large density disturbances that at times were observed to disrupt the parachute bow-shock in the Shadowgraph video. Figure 18 is an instantaneous *PIV* image also illustrating the suspension line interaction. The bow-shock appears to crawl up the suspension line, which subsequently results in a disruption of the bow-shock. The response of the parachute to this

disruption was a partial collapse of the canopy, i.e. an area oscillation. Therefore, shocks emanating from the suspension lines, in conjunction with wake to bow-shock coupling, are responsible for the area oscillation event. This is a critical finding because the original Viking parachutes used Dacron suspension lines with a thickness to nominal diameter ratio of 0.00157, similar to that of the subscale test article. We can expect this effect to be reduced for today's thinner Kevlar-line flight parachutes. Therefore, the non-dimensionalized frequency of area oscillations in the subscale test environment is a conservative representation of parachute performance on Mars. Also important to note, is the fact that the Viking era Dacron suspension lines were six times thicker than modern day Kevlar suspension lines, suggesting that suspension line interaction will be reduced for *MSL* versus a Viking era parachute of the same approximate size/load.

D. Supersonic Inflation

As mentioned previously, a high-speed camera view was used to record the supersonic inflation of the various test configurations Sleeve deployment has obvious differences from a mortar deploy, namely the absence of bag-stripping forces, but the initial presentation of the canopy skirt to the wind-stream shares similarities to a mortar deploy, making it a useful qualitative dataset for understanding the dynamics of an inflating parachute. Inflation times ranged from 9 to 15 ms from Mach 2 to 2.5 respectively. No Mach dependence was observed in terms of inflation dynamics or the un-furling process. The initial presentation and evolution of the canopy to the free-stream was similar for all configurations documented. The canopies inflated from the canopy mouth (not the gap), in spite of de-lacing from the apex forward. The most interesting feature observed during the inflation was a multi-gore in-fold present in all canopies as shown in Fig. 19. The 19.7-m *PEPP* inflation also exhibited this in-fold, suggesting it is characteristic of supersonic initial inflation[11]. Shadowgraph data were also obtained during the inflation process. Prior to the deployment sleeve's removal an attached shock emanates from the stowed parachute pack. When the sleeve is removed and the canopy inflates the shock transitions to detached. In some instances disruption of the shock occurred but it should also be noted that at no time during an inflation was an area oscillation event observed to occur. In fact, the partially inflated presentation of the canopy was very similar to an area oscillation, suggesting it be a stable shape in terms of the ability to re-inflate. Flag drag and flapping dynamics were not observed during the inflation.

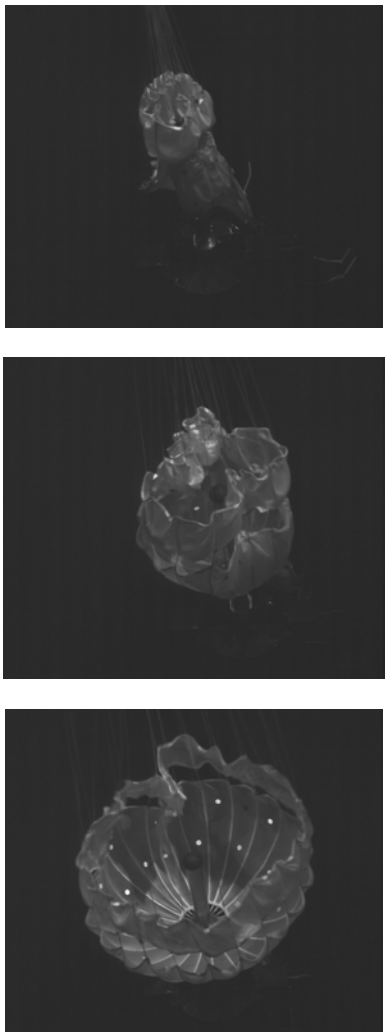

Fig. 19 Images of supersonic initial inflation at Mach 2.5. The images document, left to right, 2, 4, and 6 ms from sleeve release (deployment)[23].

V. Conclusion

The wind tunnel experiments performed have been used to determine the supersonic performance of a subscale representation of the *MSL DGB* parachute in the wake of a 70-deg sphere-cone bi-conic entry-vehicle. The Mach and Reynolds number dependence of the parachute's performance was investigated with non-intrusive diagnostic techniques including particle image velocimetry, Shadowgraph, and photogrammetric shape reconstruction from high speed video. Parachute dynamic response to the flow-field is due to a combined effect of capsule wake interaction and suspension line interaction resulting in periodic depressurization and pressurization of the canopy and resultant variation in drag and stability. The magnitude and frequency of the response were found to be a function of Mach number, Reynolds number and parachute trim angle. The parachute's drag performance was found to be consistent with the historical dataset; therefore the current model of supersonic parachute performance is adequate.

Another interesting dataset obtained was high speed video and shadowgraph of the supersonic *DGB* inflation. Inflation was orderly and consistent with no apparent dependence on Mach number or trim angle for those investigated. The parachutes were observed to inflate from the mouth and exhibited a characteristic in-fold also seen on supersonic high altitude tests, suggesting the scalability of the inflation process.

In summary, the area oscillation phenomenon was observed and characterized in terms of the frequency, severity, Mach dependence, and dynamic loading environment. The results of the test program suggest that non-dimensional aerodynamic and geometric parameters are valid in understanding the physics of supersonic *DGB* flight in the regime of interest to a Mars deployment.

Acknowledgments

The authors would like to acknowledge Dutch Slager of the Jet Propulsion Laboratory and Lance Foster, Christine Pastor, Dan Kovach, Adam Wroblewski, Randy Locke, Gary Huber Vince Anton, Roland Gregg, Matt Ogorzaly, Jordan Wagner, and the entire wind tunnel staff at the *NASA GRC* 10x10 wind tunnel, for the development and conducting of the flexible parachute test program. We would also like to acknowledge Walt Machalick, Anthony Levay, Mike Kandis, and James Reuter from Pioneer Aerospace Corp. for their work in designing the subscale parachutes and participation in the testing. The Jet Propulsion Laboratory, California Institute of Technology carried out the activities described in this paper, under a contract with the National Aeronautics and Space Administration. Copyright 2009. All rights reserved.

References

[1] D. Way, R. Powell, A. Chen, and A. Steltzner, "Asymptotic Parachute Performance Sensitivity" 2006 IEEE Aerospace Conference, Big Sky, MT, March 2006.

[2] R. Mitcheltree, .W. Lee, A. Steltzner, and A. SanMartin, ``Mars Exploration Rover Mission: Entry, Descent, and Landing System Validation,'' IAF Paper IAC-04-Q.3.a.02, October, 2004

[3] P. Hoffman, T. Rivellini, E. Slimko, N. Dahya, A. Agajanian, J. Knight, A. Sengupta, B. Thoma, R. Webster, J. Gallon, M. Gradziel, "Preliminary Design of the Cruise, Entry, Descent, and Landing Mechanical Subsystem for *MSL*," IEEE Aerospace Conference, March 3-10, 2007, Big Sky, MT.

[4] R. Mitcheltree, A. Steltzner, A. Chen, M. SanMartin, and T. Rivellini "Mars Science Laboratory Entry Descent and Landing System Verification and Validation Program," IEEE- 0-7803-9546-8/06.

[5] A. Steltzner, D. Kipp, A. Chen, P. Burkhart, C. Guernsey, G. Mendeck, R. Mitcheltree, R. Powell, T. Rivellini, M. San Martin, D. Way, "Mars Science Laboratory Entry, Descent, and Landing System", IEEAC #1497, IEEE Aerospace Conference, March 4-11, 2006, Big Sky, MT.

[6] D. Dickenson et. al., "Balloon Launched Decelerator Test Post-Flight Test Report BLDT Vehicle AV1," TR-3720289, Sept 1972.

[7] R. Ingoldby et. al., "Entry Data Analysis for Viking Landers," Feb 2002, Contractor Report (1976).

[8] D. Dickenson et. al., "Balloon Launched Decelerator Test Post-Flight Test Report BLDT Vehicle AV4," TR-3720295, Oct 1972.

[9] R.D. Moog and F.C. Michel, "BLDT Summary Report,"TR-372039,March 1973.

[10] A. Sengupta, A. Steltzner, A. Witkowski, and J. Rowan, "An Overview of the Mars Science Laboratory Parachute Decelerator System," IEEE-1432-2007, March 2007.

[11] H. Murrow and J. Mcfall, "Some Test Results from the *NASA* Planetary Entry Parachute Program," *J. Spacecraft*, Vol. 6 (5): 621-623, 1969.

[12] D.E Reichenau., "Aerodynamic Characteristics of Disk-Gap-Band Parachutes in the Wake of Viking Entry Forebodies at Mach Numbers from 0.2 to 2.6," AEDC-TR-72-78, Arnold AFB, Tennessee, (1972).

[13] L. Couch, "Drag and Stability Characteristics of a Variety of Reefed and Un-Reefed Parachute Configurations at Mach 1.8 with an Empirical Correlation for Supersonic Mach numbers," *NASA* TR R-429, February 1975.

[14] A. Sengupta et. al., "Results from the Mars Science Laboratory Parachute Decelerator System Supersonic Qualification Program," IEEE-1435-2008, March 2008.

[15] A. Sengupta et. al, "Supersonic Qualification Program for the Mars Science Laboratory Parachute Decelerator System," AIAA 2007-2542, May 2007.

[16] A. Sengupta et. al., "Findings from the Supersonic Qualification Program of the Mars Science Laboratory Parachute System," AIAA-2009-2900, May 2009.
[17] M. Barnhardt, T. Drayna, Ioannis Nompelis, G.V. Candler, and W. Garrard, "Detached Eddy Simulations of the *MSL* Parachute at Supersonic Conditions," AIAA-2529-2007, May 2007.
[18] http://facilities.*GRC.NASA*.gov/documents/TOPS/Top10x10.pdf , "10- by 10-Foot Supersonic Wind Tunnel," TOP3-00226, Jan 2007.
[19] V. Gidzak et. al., "Simulation of Fluid-Structure Interaction of the Mars Science Laboratory Parachute," AIAA 2008-6910, August 2008.
[20] K. Equist et. al., "Mars Science Laboratory Entry Capsule Aerothermodynamics and Thermal Protection System," IEEE-1423-2007, March 2007.
[21] A. Witkowski, M. Kandis, J. Reuter and W. Machalick, R. Kelsch, "Design of Subscale Parachute Models for *MSL* Supersonic Wind Tunnel Testing," AIAA-2009-2999, May 2009.
[22] E. Niemi, "An Improved Canopy Stiffness Scaling Law For Determining Opening Time of Flat Circular Parachutes," AIAA-90-3058-CP,
[23] A. Sengupta et. al., "Supersonic Disk Gap Band Parachute Performance in the Wake of a Viking-Type Entry Vehicle from Mach 2 to 2.5," AIAA-2008-6217, Presented at the AIAA Atmospheric Flight Mechanics Conference, Honolulu, HI, Aug 18-21 2008.
[24] I. Jaremenko, S. Steinberg, and R. Faye-Petersen, "Scale Model Test Results of the Viking Parachute System at Mach Numbers from 0.1 Through 2.6," TR-3720181, November 1971.
[25] Soloff, S.M., Adrian, R.J., and Liu, Z-C, "Distortion Compensation for Generalized Stereoscopic Particle Image Velocimetry," Measurement Science and Technology, Vol. 8, No. 12, pp. 1441-1454, 1997.
[26] Bjorkquist, D.C., "Design and Calibration of a Stereoscopic *PIV* System," Proc. 9th International Symposium on Applications of Laser Techniques to Fluid Mechanics, Vol. 1, pp. 6.5.1-6.5.8, Lisbon, Portugal, 1998.
[27] M. Wernet et. al., "Application of Stereo *PIV* on a Supersonic Parachute Model," AIAA-0070-2009, Presented at the 47th AIAA Aerospace Sciences Conference, Orlando, FL Jan 2009.
[28] Wernet, M. P., "Symmetric Phase Only Filtering: a New Paradigm for DPIV Data Processing", *Meas. Sci. Technology*, 16, pp. 601-618, 2005.